Optics Letters

On-demand polarization by a vertical-cavity surface-emitting laser with two tilted sub-wavelength gratings

Valerio Torrelli,[1,2,†] Martino D'Alessandro,[1,2,†,*] Wolfgang Elsäßer,[3,4,5] and Pierluigi Debernardi[1]

[1] Istituto di elettronica e di ingegneria dell'informazione e delle telecomunicazioni (IEIIT) del Consiglio Nazionale delle Ricerche (CNR), Politecnico di Torino, Torino 10129, Italy
[2] Department of Electronics and Telecommunications (DET), Politecnico di Torino, Corso Duca degli Abruzzi, 24, Torino 10129, Italy
[3] Institute of Applied Physics, Technische Universität Darmstadt, Schlossgartenstrasse 7 Darmstadt 64289, Germany
[4] School of Physics, Trinity College Dublin, Dublin 2, Ireland
[5] Associated with Istituto di elettronica e di ingegneria dell'informazione e delle telecomunicazioni (IEIIT) del Consiglio Nazionale delle Richerche (CNR), Politecnico di Torino, Torino 10129, Italy
† These authors contributed equally to this work.
*martino.dalessandro@polito.it

Received 26 April 2024; revised 3 June 2024; accepted 10 June 2024; posted 10 June 2024; published 27 June 2024

We show that each polarization state on the Poincaré sphere (PS) can be accessed on-demand (Poincaré sphere tailoring) by a semiconductor-based vertical-cavity surface-emitting laser (VCSEL) with two tilted sub-wavelength gratings (SWGs). We develop a vectorial Barkhausen criterion that answers the question: what conditions must the cavity fulfill to support a given desired polarization state? Addressing this inquiry leads to a completely different strategy based on the entangled interplay between two tilted SWGs, resulting in an overall chiral cavity, whose features depend on the gratings and their mutual rotation. This leads to the emission of a well-controllable polarization state based on standard technologies used in polarization-stable VCSELs, which paves the way for inspiring several new potential applications. © 2024 Optica Publishing Group. All rights, including for text and data mining (TDM), Artificial Intelligence (AI) training, and similar technologies, are reserved.

https://doi.org/10.1364/OL.528268

Introduction. Vertical-cavity surface-emitting lasers (VCSELs) have become technologically mature and highly sophisticated optoelectronic emitters. They are nowadays one of the most important semiconductor lasers, dominating the high-speed datacom [1] and sensing markets [2]. Among others, quantum optic applications, such as atomic clocks [3] and quantum gyroscopes [4], represent a hot topic. One key question at the advent of VCSELs concerned the polarization of the emitted optical field. Due to their cylindrical rotational symmetry and their in-plane quantum well isotropic gain, an undetermined polarization was first expected. However, the intrinsic semiconductor electro- and elasto-optic anisotropies [5] lead to a linear polarization operation, with many kinds of polarization switching and instabilities [6,7], detrimental for sensing applications. For that reason, strong efforts that lasted for two decades finally resulted in a simple and effective technique to achieve polarization-stable VCSEL operation: etching a surface grating oriented along the crystalline axes, first proposed by our group in [8] and soon after demonstrated by experimental results [9–11]. Since then, gratings have become the standard way of fixing VCSELs' polarization, with improved performance introduced by sub-wavelength gratings (SWGs) [12].

Recently, circular polarization has become an enabling feature in many advanced quantum photonic applications [13–15]. The common non-monolithic approach to achieving circular polarization uses a linearly polarized VCSEL and a quarter-wave plate, which is a bulky solution that invalidates the small VCSEL footprint. Many efforts have been made to achieve well-controlled circularly polarized VCSEL emission by compact monolithic solutions [16]. To the best of our knowledge, two different compact solutions have been proposed so far, both based on introducing one single chiral component in the resonator, namely, either a cholesteric liquid crystal [17] or a chiral metamaterial layer [18–21]. This approach was deployed in [22], with a novelty compared to previous implementations: the chiral structure also contributes to the reflectivity of the top mirror, achieving at most 60% of circularly polarized light. All the previous techniques present drawbacks. For instance, liquid crystals require non-standard and non-monolithic technologies, which resulted in successful experimental validation only in a few cases [23].

Here we follow a different approach, by moving the focus from the chirality of a single cavity component to the chirality of the whole resonator. The resonator chirality, the property by which an object or structure and its mirror image are not superimposable, plays a key role [24] to depart from linear polarization emission. We use anisotropic layers, *per se* achiral, if considered singularly, that make the overall cavity chiral when their anisotropic axes are tilted against each other and interact within the resonator round trip loop.

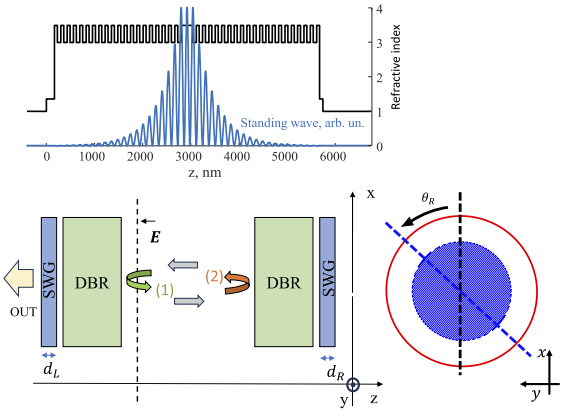

Fig. 1. Top: refractive index and standing wave profile of our VCSEL structure. The structure designed for a wavelength of 850 nm features a λ-cavity, two symmetric 20-pair $\lambda/4$ DBRs terminated by sub-wavelength surface gratings (SWGs). The high and low values of the refractive index are chosen to be $n_H = 3.5$ and $n_L = 3$, respectively. Bottom: schematics of the cavity to be investigated within the Barkhausen round trip cavity framework with the orientation of the tilted gratings (right).

Modeling. We investigate our idea at the most basic level by the VCSEL structure shown in Fig. 1. In the top part, we depict its refractive index and standing wave profile for a specific SWG parameter set. In the lower part, we report a schematic of the VCSEL resonator and the definition of the coordinate reference system. The main focus is to sketch the derivation of an agile and effective mathematical framework (Barkhausen criterion), to be used for on-demand polarization control in VCSELs. To that end, we choose the simplest possible VCSEL, placing the SWGs at the end of both DBRs, so that the two chirality enablers are the most far away as possible. All the intrinsic anisotropies, such as the electro-optic and elasto-optic ones, are neglected. Indeed, they are relevant in real-world VCSELs but not needed to explain the principle of operation of our chiral device. A realistic and technologically compliant device was simulated for comparison by our 3D electromagnetic solver VCSEL ELectroMagnetic Suite (VELMS-3D) [5,8,10,25], including the intrinsic anisotropies, thereby confirming the trends of this work.

We summarize the theory describing polarization modes supported by a 1D chiral resonator. We write the phasor representation of the electric field in the resonator as follows:

$$\mathcal{E}(t) = \Re\{(E_x\hat{x} + E_y\hat{y})e^{i\omega t}\} = \Re\{E_y(\chi\hat{x} + \hat{y})e^{i\omega t}\}, \quad (1)$$

where $E_x\hat{x} + E_y\hat{y} = \mathbf{E}$ is the complex electric field phasor, $\mathcal{E}$ is its real time-dependent counterpart (vectors and matrices are represented by bold fonts), and the polarization χ-index is defined as $\chi := E_x/E_y$. To understand why χ fully represents the polarization features, notice that the effect of any multiplicative complex constant (E_y in Eq. (1)) results in an overall phase shift and a uniform scaling factor, both irrelevant to the polarization characteristics [26]. In this view, the overall field phasor is represented by $\chi\,\hat{x} + \hat{y}$ without loss of generality. The polarization state of the light is generally characterized by the Stokes parameters [27,28], which are conveniently mapped onto the Poincaré sphere (PS) [29,30]. This representation is isomorphic to the χ-index via a stereographic projection (similar considerations were done for qubit states in [31]), obtained by substituting the phasor $\chi\hat{x} + \hat{y}$ in the definition of the Stokes parameters as follows:

$$\begin{aligned} S_0 &= |E_x|^2 + |E_y|^2 = |\chi|^2 + 1 > 0, \\ S_1 &= \frac{|E_x|^2 - |E_y|^2}{S_0} = \frac{|\chi|^2 - 1}{S_0} \in [-1, +1], \\ S_2 &= \frac{+2\Re\{E_y^* E_x\}}{S_0} = \frac{+2\Re\{\chi\}}{S_0} \in [-1, +1], \\ S_3 &= \frac{-2\Im\{E_y^* E_x\}}{S_0} = \frac{-2\Im\{\chi\}}{S_0} \in [-1, +1]. \end{aligned} \quad (2)$$

To derive the Barkhausen condition [32] for the cavity in Fig. 1, one must generalize the concept of scalar reflection coefficient to 2D reflection matrices [33], as usually done in the Jones formalism [26,29]. The reflection and transmission matrices of the left DBR mirror (and similarly for the right one) terminated by a grating whose bars are aligned with the chosen reference system can be written as follows:

$$\mathbf{\Gamma}_L = \begin{bmatrix} \Gamma_L^x & 0 \\ 0 & \Gamma_L^y \end{bmatrix}, \quad \mathbf{T}_L = \begin{bmatrix} T_L^x & 0 \\ 0 & T_L^y \end{bmatrix}. \quad (3)$$

SWGs are exactly treated with rigorous coupled-wave analysis [34,35], here approximated by uniform anisotropic layers according to the Born–Wolf formulation [36] with anisotropic indices $n_x = 1.30$ and $n_y = 2.57$ (50% filling factor). The overall reflectivities that appear in Eq. (3) are computed by combining the scattering matrices of the single gratings and the DBR stack. Two different reflection coefficients result depending on the orientation of the impinging electric field, either parallel or perpendicular to the grating bars. With a single grating, it is a natural choice to use the orthogonal reference system defined by its bars. When a second grating is added (the right one in our case), its reflection matrix can be written as follows:

$$\mathbf{\Gamma}_R = \mathbf{R}^{-1}\mathbf{\Gamma}_R\mathbf{R}, \quad \text{where} \quad \mathbf{R} = \begin{bmatrix} \cos\theta_R & -\sin\theta_R \\ \sin\theta_R & \cos\theta_R \end{bmatrix}. \quad (4)$$

The matrix $\mathbf{R}$ represents a change of the reference system from the one of the left grating to the one defined by the right one. θ_r is the tilting angle of the right grating with respect to the left one (Fig. 1, bottom right).

The vectorial Barkhausen condition is derived with reference to Fig. 1 on the backward field component at the left interface. By choosing the depicted round trip path, we first apply the reflection on the left mirror, and then the one on the right, resulting in the following:

$$\Big[\mathcal{P}\mathbf{D} - \mathbf{I}\Big]\mathbf{E} = 0, \quad \text{where} \quad \mathbf{D} = \mathbf{R}^{-1}\mathbf{\Gamma}_R\mathbf{R}\mathbf{\Gamma}_\mathbf{L}, \quad (5)$$

$$\text{with} \quad \mathcal{P}(k, g) = \exp\Big((g\Gamma_z + i2k)L\Big). \quad (6)$$

In Eq. (5), $\mathbf{I}$ is the identity matrix and in Eq. (6), $\mathcal{P}$ represents the cavity propagator: L is the cavity length, $k = \frac{2\pi}{\lambda}n_H$, λ is the emission wavelength, g is the power gain of the quantum well with thickness $d = 10$ nm assumed to be at the center of the cavity, and I is the identity matrix. The overlap between the electric field and the quantum well is described by Γ_z, which in our configuration can be approximated as $\frac{2d}{L}$. We name $\mathbf{D}$ as the roto-reflection matrix. It contains all the information about the mirrors and, in general, depends on k because of mirror dispersion.

A matrix can be classified as chiral or achiral depending on whether it can be diagonalized by two complex or real eigenvectors, respectively. An achiral matrix can be always represented by a diagonal matrix in the proper reference system; this is the case of a grating mirror [see Eq. (3)]. This reference system is the one defined by the eigenvector directions. To achieve elliptical polarization in lasers, the important requirement is the chirality of the overall resonator, namely, of the roto-reflection matrix **D**.

In literature, to the best of our knowledge, this has been achieved by introducing a chiral layer in one of the mirrors [22]. In this work, instead, we propose a novel approach that allows breaking the symmetry of the cavity with two combined tilted achiral mirrors. In this way, the overall roto-reflection matrix **D** is chiral, and therefore supports complex eigenvectors, corresponding to any kind of elliptical polarization, including the circular one. Exploiting Eq. (5), we can write the following:

$$\begin{cases} \mathcal{P}D_{11}\chi + \mathcal{P}D_{12} = \chi \\ \mathcal{P}D_{21}\chi + \mathcal{P}D_{22} = 1. \end{cases} \tag{7}$$

Multiplying the second line by χ and equating the left-hand sides, we can drop $\mathcal{P}$. Furthermore, ascertaining a negligible mirror dispersion, we can evaluate the terms D_{ij} at the design wavelength ending up with a decoupled equation only describing polarization, namely, the polarization equation:

$$D_{21}\chi^2 + (D_{22} - D_{11})\chi - D_{12} = 0. \tag{8}$$

Its roots $\chi_{1,2}$ represent the polarization of the two modes supported by the cavity. Plugging back the roots $\chi_{1,2}$ into the first equation of Eq. (7), it is possible to obtain the $\mathcal{P}$ values associated with $\chi_{1,2}$, in turn yielding the modal threshold gains and the emission wavelengths from $|\mathcal{P}|$ and $\angle\mathcal{P}$ according to Eq. (6). The lasing polarization is the one associated with the lowest threshold gain, described in the following section. The χ-parameter at the output is calculated as $\chi_{out} = \left(T_L^x/T_L^y\right)\chi$. By exploring the SWG parameter space by varying the grating thicknesses d_L and d_R and the tilting angle θ_R, one can investigate the features of the emitted polarization.

Results and discussion. As a first investigation, the output polarization index χ_{out} and its projection onto the Poincaré sphere according to Eq. (2) were determined for wide ranges of grating parameters, namely, $\theta_R \in [1, 179]^\circ$, $d_L \in [20, 400]$ nm, and $d_R \in [50, 130]$ nm. As a key result, the whole Poincaré sphere was accessed, showing how any polarization can be obtained on-demand in dependence on the SWG parameters as depicted in Fig. 2. We focus now our attention to circularly polarized light, a case of particular interest in several applications. To this aim, we select a fixed right grating thickness $d_R = 70$ nm and vary the other two parameters d_L and θ_R, resulting in the map depicted in Fig. 3. The map on the left displays the values of S_3, showing a wide range for which it approaches the desired value of 1. For a more quantitative visualization, Fig. 3 (right) reports cuts of the previous map at the value of d_L associated with the maximum S_3. This is reported not only for $d_R = 70$ nm but also for two additional grating thicknesses, demonstrating that it is still possible to reach $S_3 = 1$ even with different d_R values.

The nearly perfect agreement between our results and those computed with our one-dimensional version of the VCSEL ELectroMagnetic Suite, VELMS-1D [25], reported by the squares in Fig. 3 (right), provides full validation of our vectorial Barkhausen formalism and the soundness of the dispersionless approximation, not assumed in VELMS-1D. We infer interesting information in the examined range of d_R. $S_3 = 1$ is obtained for $d_L = 167.5$ nm and $\theta_R = 49^\circ$; S_3 remains above 0.95 within a tilting range of $\pm 10^\circ$ around the target value. For lower and higher d_R, $S_3 = 1$ occurs at smaller tilting angles. For both values, the sensitivity to the grating tilting angle is stronger. At the same time, the threshold difference becomes smaller, but

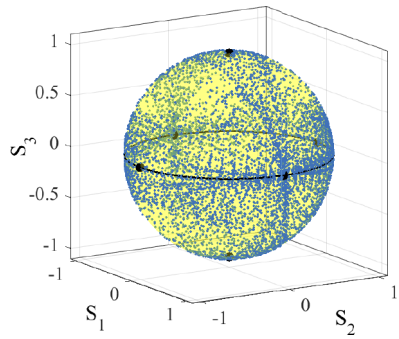

Fig. 2. Graphical depiction of accessing all polarization states on the full Poincaré sphere by spanning $\theta_R \in [1, 179]^\circ$ with 50 points, d_L varying from 20 to 400 nm in steps of 10 nm, and $d_R \in [50, 70, 100, 130]$ nm, yielding 7800 points in total.

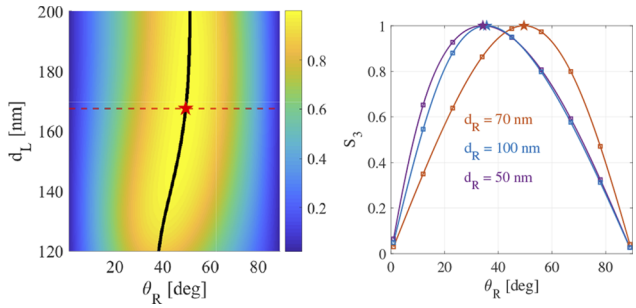

Fig. 3. Left: color density plot of S_3 versus d_L and θ_R for $d_R = 70$ nm. The red dashed line is the cut at the d_L grating thickness that ensures $S_3 = 1$ ($S_3 = 1$ at the star). The black line is the θ_R at which the S_3 is the maximum for each d_L value. Right: S_3 versus θ_R for three values $d_R = 50$, 70, and 100 nm. The red curve is the cut on the left for $d_L = 167$ nm. Similarly, for maps computed for $d_R = 50$ and 100 nm, we observe $S_3 = 1$ (stars) for $d_L = 141$ and 199 nm. The squares represent the values obtained with VELMS-1D.

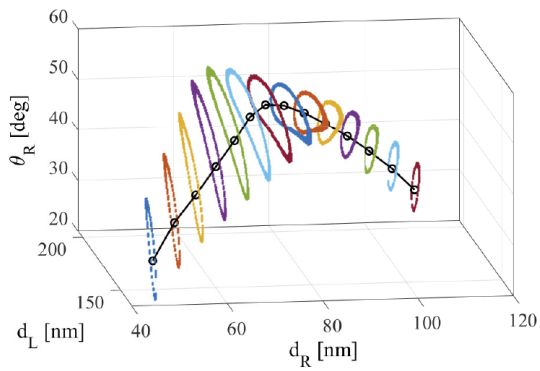

Fig. 4. Circular polarization design chart. $S_3 = 1$ trajectory [iso-circular-polarization (ICP) line] in the 3D parameter space and the regions featuring $S_3 \geq 0.99$ within the colored lines.

still sufficient to guarantee a single-mode operation. In Fig. 4, we provide the complete parameter space investigation. The black curve in the 3D space of grating thicknesses and relative angle (d_L, d_R, and θ_R) shows the trajectory where $S_3 = 1$, i.e., the iso-circular-polarization (ICP) line, while the colored dots around it define the boundaries of the region for which $S_3 \geq 0.99$. Overall, we can see that the tolerance for θ_R is always at least ±5°. Moreover, we observe a large insensitivity to d_L, maximum for d_R =70 nm (the case investigated also in Fig. 3), but pretty much the same in the whole range $60<d_R<80$ nm. In summary, we can achieve S_3=1 in a very broad range of grating thicknesses: $40<d_R<100$ nm and $130<d_L<210$ nm, with tilting angles from 25 to 50°. The better performance in terms of parameter insensitivity is at the center of those intervals, where the tilting angle is around 45°, which allows the highest coupling of the x and y polarizations. For increasing grating thicknesses, beyond the ones investigated in Fig. 3 (left), one reaches a region of $S_3 = -1$ (counterclockwise circular polarization). After that, the phenomenon shows periodic features. Of course, from a technology perspective, it is better to operate at the minimum grating thickness, namely, the region explored in Fig. 4, which can be regarded as a design look-up table for circularly polarized VCSELs. $S_3 = -1$ is achieved by the same grating designs of Fig. 4, but opposite tilting angle. In this way, one might have on the same chip, close to each other, two VCSELs emitting $S_3 = \pm 1$.

Conclusions and outlook. We propose for the first time a straightforward approach to realize chirality in a VCSEL by combining two SWGs tilted against each other. This is feasible by exploiting the mature SWG technology. This tilt enables the coupling of the two otherwise decoupled polarization channels, x and y, which results in a completely new approach for the achievement of chirality. Here, the overall VCSEL chirality is obtained by combing two anisotropic *per se* achiral layers, whereas on the contrary, earlier proposals always suggested to embed in the resonator a single and *per se* chiral layer. We investigated this novel chiral cavity by a vectorial Barkhausen condition, deriving analytical formulas for the supported polarization modes, showing that we can access any on-demand polarization by varying the SWG design parameters. Among all possible polarizations, we targeted the generation of fully circularly polarized light, suggesting affordable technological implementations for circularly polarized nearly standard monolithic VCSELs and paving the way toward a plethora of exciting new applications.

Acknowledgment. We appreciate the discussion within the Center of Excellence (CoE) "VCSELence Torino," Dr. Alberto Tibaldi and Prof. Renato Orta. This work was supported by NRRP Grant PE00000001—Program RESTART, Project RIGOLETTO.

Disclosures. The authors declare no conflicts of interest.

Data availability. Data underlying the results presented in this paper are not publicly available at this time but may be obtained from the authors upon reasonable request.

REFERENCES

1. B. D. Padullaparthi, J. A. Tatum, and K. Iga, *VCSEL Industry - Communication and Sensing*, 1st ed. (John Wiley & Sons, 2022).
2. G. K. Veerabathran, S. Sprengel, A. Andrejew, *et al.*, Appl. Phys. Lett. **110**, 071104 (2017).
3. L. S. Watkins, C. Ghosh, J.-F. Seurin, *et al.*, Proc. SPIE **9616**, 96160J (2015).
4. Y. Zhou, Y. Jia, X. Zhang, *et al.*, Opt. Express **30**, 8991 (2022).
5. P. Debernardi, G. P. Bava, C. Degen, *et al.*, IEEE J. Quantum Electron. **38**, 73 (2002).
6. J. Martin-Regalado, F. Prati, M. San Miguel, *et al.*, IEEE J. Quantum Electron. **33**, 765 (1997).
7. K. Panajotov and F. Prati, *Springer Series in Optical Sciences* (Springer, 2013), pp. 181–231.
8. P. Debernardi and G. P. Bava, IEEE J. Select. Topics Quantum Electron. **9**, 905 (2003).
9. J. M. Ostermann, P. Debernardi, C. Jalics, *et al.*, Proc. SPIE **5364**, 528237 (2004).
10. P. Debernardi, J. Ostermann, M. Feneberg, *et al.*, IEEE J. Sel. Top. Quantum Electron. **11**, 107 (2005).
11. P. Debernardi, J. M. Ostermann, M. Sondermann, *et al.*, IEEE J. Sel. Top. Quantum Electron. **13**, 1340 (2007).
12. A. Haglund, J. Gustavsson, J. Bengtsson, *et al.*, IEEE J. Quantum Electron. **42**, 231 (2006).
13. A. Z. Goldberg, P. de la Hoz, G. Björk, *et al.*, Adv. Opt. Photonics **13**, 1 (2021).
14. R. Farshchi, M. Ramsteiner, J. Herfort, *et al.*, Appl. Phys. Lett. **98**, 162508 (2011).
15. C.-J. Yu, C.-E. Lin, L.-P. Yu, *et al.*, Appl. Opt. **48**, 758 (2009).
16. A. Maksimov, E. Filatov, I. I. Tartakovskii, *et al.*, Phys. Rev. Appl. **17**, L021001 (2022).
17. X. Zhan, F. Xu, Z. Zhou, *et al.*, Adv. Mater. **33**, 2104418 (2021).
18. Y. Zhu, F. Zhang, G. You, *et al.*, Appl. Phys. Express **5**, 032102 (2012).
19. M. Kang and J. Chen, Opt. Express **32**, 13357 (2024).
20. Z. Yuan, S.-H. Huang, Z. Qiao, *et al.*, Optica **10**, 269 (2023).
21. K. Voronin, A. S. Taradin, M. V. Gorkunov, *et al.*, ACS Photonics **9**, 2652 (2022).
22. X. Jia, J. Kapraun, J. Wang, *et al.*, Optica **10**, 1093 (2023).
23. B. Boisnard, C. Levallois, C. Paranthoen, *et al.*, IEEE Photonics Technol. Lett. **32**, 391 (2020).
24. L. Cerdán, S. García-Moreno, A. Costela, *et al.*, Sci. Rep. **6**, 28740 (2016).
25. V. Torrelli, A. Gullino, A. Tibaldi, *et al.*, IEEE Photonics J. **16**, 0600507 (2024).
26. B. E. A. Saleh and M. C. Teich, *Fundamentals of Photonics* (Wiley, 1991).
27. G. G. Stokes, Trans. Cambridge Philos. Soc. **9**, 399 (1852).
28. A. Molitor, S. Hartmann, and W. Elsässer, Opt. Lett. **37**, 4799 (2012).
29. E. Collett, *Polarized Light: Fundamentals and Applications* (Marcel Dekker, 1993).
30. D. H. Goldstein, *Polarized Light* (CRC Press, 2017).
31. H. Kobayashi, K. Nonaka, and Y. Shikano, Phys. Rev. A **89**, 053816 (2014).
32. P. Salzenstein and E. Pavlyuchenko, Int. J. Simul. Multidisci. Des. Optim. **11**, 24 (2020).
33. R. Orta, A. Tibaldi, and P. Debernardi, IEEE J. Quantum Electron. **52**, 6100508 (2016).
34. M. G. Moharam and T. K. Gaylord, J. Opt. Soc. Am. **71**, 811 (1981).
35. L. Li, J. Opt. Soc. Am. A **13**, 1870 (1996).
36. M. Born and E. Wolf, *Principles of Optics: 60th Anniversary Edition* (Cambridge University Press, 2019).